Friction drag reduction through damping of the near-wall spanwise velocity fluctuation

Bettina Frohnapfel[a], Yosuke Hasegawa[b], Nobuhide Kasagi[b]

[a] *Center of Smart Interfaces, Technical University of Darmstadt, Germany*
[b] *Dept. of Mechanical Engineering, The University of Tokyo, Japan*

Abstract

Direct numerical simulation (DNS) of a turbulent channel flow is performed in order to explore the possibility of reducing wall friction drag and saving energy through damping of the spanwise velocity fluctuation. Starting from an idealized feedback control, we extend the idea to a practically realizable control, in which only the streamwise wall shear stress is required as sensor input, while actuators of finite size are employed. This control scheme offers drag reduction of up to 20%, which is the highest value achieved by existing feedback controls based on the streamwise wall shear stress. In addition, the control power input remains two orders of magnitude smaller than the pumping power for the uncontrolled flow.

Key words: turbulent channel flow, viscous drag reduction, active flow control

1. Introduction

Turbulence control techniques leading to skin friction drag reduction are of great economical and ecological interest. In general, active feedback control schemes offer potentially large energy saving that can be obtained with small power input. Choi et al. (1994) first proposed the so-called opposition control, in which blowing/suction velocity is given at the wall so as to oppose the velocity components at a virtual detection plane located above the

Email addresses: frohnapfel@csi.tu-darmstadt.de (Bettina Frohnapfel), hasegawa@thtlab.t.u-tokyo.ac.jp (Yosuke Hasegawa), kasagi@thtlab.t.u-tokyo.ac.jp (Nobuhide Kasagi)

wall. They obtained about 25% drag reduction in their direct numerical simulations at low Reynolds numbers. In real systems, however, the available turbulent state information is practically limited to variables measured at the wall such as the streamwise wall shear stress, $\tau_x = \mu(\partial u_1/\partial x_2)_w$, the wall pressure, p_w, and the spanwise wall shear stress, $\tau_z = \mu(\partial u_3/\partial x_2)_w$. According to DNS studies, the control algorithms using τ_z or p_w are very effective (Lee et al., 1997; Lee et al., 1998; Koumoutsakos, 1999). These quantities, however, are in most cases difficult to measure by using small sensors distributed on the wall so that a control scheme based on τ_x is strongly required from a practical point of view (Kasagi et al., 2009).

Recently, Fukagata and Kasagi (2004) applied a suboptimal control theory with a cost function based on the near-wall Reynolds shear stress, which is directly related to the friction drag (Fukagata et al., 2002). As a result, they developed a control law which requires τ_x only. Morimoto et al. (2002) used a genetic algorithm (GA) to optimize weights in a prescribed function, which determines an actuator's movement from the streamwise wall shear signals measured at multiple spanwise locations. In both cases, they employed blowing/suction from the wall as control input and achieved drag reduction of about 10%, which is smaller than the value attained by the above-mentioned control algorithms based on τ_z or p_w.

It is known that suppressing the spanwise velocity, $w = u_3$, near the wall leads to substantial drag reduction as reported in Satake and Kasagi (1996) (SK) and Lee and Kim (2002) (LK). The resultant control performance was found to be similar or even superior to that achieved by suppressing the wall-normal velocity fluctuation (Choi et al., 1994).

In the present work, this "w-damping" is revisited to develop an efficient control algorithm based on τ_x only and investigate the possibility of implementing it to a more realistic control scheme. Plasma actuators and Lorentz forces generally allow the introduction of tangential forces, but up to now no effective feedback scheme based on the w-damping concept is available.

2. Numerical Procedures

We carry out DNS of a fully developed channel flow with a constant flow rate. The bulk Reynolds number, $Re_b = U_b\delta/\nu$, is set to be 2228, 5055 and 8034 which corresponds to the friction Reynolds number of $Re_\tau = u_\tau\delta/\nu =$ 150, 300 and 450, respectively in the uncontrolled case, where U_b is the bulk velocity, u_τ is the friction velocity and ν and δ are the kinematic viscosity

Table 1: Computational box, number of modes and grid spacings (FDM: finite difference method, PSM: pseudo-spectral method)

Re_τ	Scheme	L_x	L_z	N_x, N_y, N_z	Δx^+	Δy^+	Δz^+
150	FDM	$2.5\pi\delta$	$\pi\delta$	64, 129, 64	18.4	0.188 - 5.7	7.4
	FDM-fine	$2.5\pi\delta$	$\pi\delta$	128, 129, 128	9.2	0.188 - 5.7	3.7
	FDM-long	$5.0\pi\delta$	$\pi\delta$	128, 129, 64	18.4	0.188 - 5.7	7.4
	PSM	$2.5\pi\delta$	$\pi\delta$	64, 97, 64	18.4	0.080 - 4.9	7.4
	PSM-large	$5.0\pi\delta$	$2.0\pi\delta$	128, 97, 128	18.4	0.080 - 4.9	7.4
300	PSM	$2.5\pi\delta$	$\pi\delta$	128, 193, 128	18.4	0.040 - 4.9	7.4
450	PSM	$2.5\pi\delta$	$\pi\delta$	192, 257, 192	18.4	0.034 - 5.5	7.4

and the channel half height, respectively. The present DNS is performed by a finite volume method on a staggered grid including a non-uniform mesh with a hyperbolic tangent distribution in the x_2-direction and a pseudo-spectral method (essentially the same as that of Kim et al. (1987)) with Fourier transforms in the x_1- and x_3-directions, and Chebyshev polynomials in x_2-direction. The no-slip condition is imposed at the wall.

For time advancement the Adams-Bashforth scheme is used for the convection terms and the Crank-Nicolson scheme for the viscous terms. The computational box, as shown in figure 1, is set to be $L_x = 2.5\pi\delta$ and $L_z = \pi\delta$ following Iwamoto et al. (2002). The computational conditions are summarized in Table 1. The grid resolution is determined so as to keep the same grid spacing in all cases. We have confirmed that doubling the grid number in streamwise and spanwise direction (FDM-fine) does not significantly affect the results shown in this paper. The computational time step is chosen as $\Delta t^+ = 0.03$ and the initial condition is given by a fully-developed velocity field of a preceding channel flow DNS. It was confirmed that the obtained turbulent statistics are in good agreement with the previous DNS data of Moser et al. (1999) and also the web page at http://www.thtlab.t.u-tokyo.ac.jp.

When the wall shear stress is decreased due to control, the size of the computational box based on wall units of the controlled flow is decreased. Therefore, there exists a possibility that the present results depend on the domain size. This becomes more important at low Reynolds number. In the present study, we conducted additional computations for typical cases

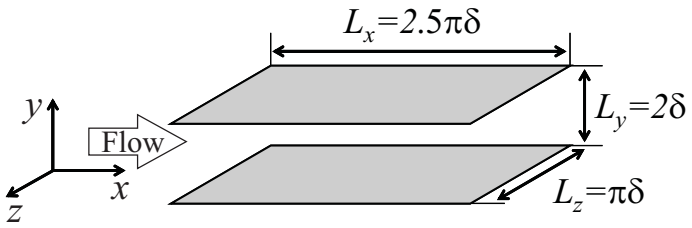

Figure 1: Computational domain.

at $Re_\tau = 150$ with a larger computational box in order to ensure that the domain size does not affect the results. The results shown in the paper correspond the the uncontrolled case of $Re_\tau = 150$ unless otherwise specified.

As a control input for damping the spanwise velocity fluctuation, we consider a feedback body force, bf_3, which is introduced into the Navier-Stokes equations. The modified spanwise momentum equation thus reads:

$$\frac{\partial u_3^+}{\partial t^+} + u_j^+ \frac{\partial u_3^+}{\partial x_j^+} = -\frac{\partial p^+}{\partial x_3^+} + \frac{\partial^2 u_3^+}{\partial x_j^+ \partial x_j^+} + bf_3^+. \tag{1}$$

A detailed formulation of bf_3 will be described in the following sections.

3. Performance Indices

For active flow control techniques, the control performance with respect to energy saving is captured with different indices. For a constant mass flow the pumping power, P, is given as a function of the average streamwise wall shear stress, $\overline{\tau_x}$, and the bulk flow velocity, U_b:

$$P = 2\overline{\tau_x} U_b. \tag{2}$$

Therefore, the reduction of pumping power is equivalent to drag reduction, R:

$$R = 1 - \frac{\overline{\tau_x}}{(\overline{\tau_x})_0} = \frac{P_0 - P}{P_0}, \tag{3}$$

where the index $()_0$ denotes the uncontrolled flow. The additional power input due to the applied control can be obtained by including the body force

in the energy equation of the flow field. For the present case it is given by:

$$P_{in} = \int_0^H \left| \underbrace{\frac{1}{TL_xL_z} \int_0^T \int_0^{L_z} \int_0^{L_x} bf_3u_3 dxdzdt}_{P_3} \right| dy, \tag{4}$$

where H corresponds to the channel height, while L_x and L_z are the lengths of the computation domain in the $x-$ and $z-$directions. P_3 denotes the local power input which will be discussed further in section 5.

The net energy saving rate, S, is given by:

$$S = \frac{P_0 - (P + P_{in})}{P_0} = R - \frac{P_{in}}{P_0}. \tag{5}$$

Note that the net energy saving rate S defines the upper limit of energy saving when neglecting all possible energy losses in the control system. In a real system, however, there always exist energy losses associated with actuators, sensors, control circuits and so forth. Suppose we define the total efficiency of the control system as η, a real energy saving rate S_{real} becomes:

$$S_{real} = \frac{P_0 - (P + P_{in}/\eta)}{P_0}. \tag{6}$$

In order to achieve net energy saving in a real system, i.e., $S_{real} > 0$, the following condition should be met:

$$G = \frac{P_0 - P}{P_{in}} > \eta^{-1}, \tag{7}$$

where G is the gain representing pumping energy saving per control input. Now, it is obvious that G determines the lower bound of η for net energy saving in a real system. Therefore, regardless of the magnitude of S, G needs to be much larger than unity to compensate possible energy losses in hardware components.

Due to the very small absolute values of P_{in} for the presented control scheme, small uncertainties in its numerical computation introduce large relative errors in the estimation of G. Therefore, the energy gain, G, should be considered an order of magnitude statement only. We note that the difference in G obtained by two different numerical schemes, i.e., finite volume and pseudo-spectral methods, are about 20% while the differences in R and S are less than 2%.

4. Ideal w-Damping

4.1. Applied body force

For the idealized w-damping, the body force bf_3 is assumed to be proportional to the instantaneous spanwise velocity:

$$bf_3^+ = -\frac{f(x_2^+)}{\Phi^+} u_3^+. \tag{8}$$

The constant Φ has the unit of time and can be interpreted as a forcing time constant. In the present study we do not investigate the dynamic behavior of the control but the fully developed state of the controlled flow. Therefore, Φ determines the strength of the forcing while $f(x_2^+)$ is a step function which defines the damping layer on top and bottom wall, such that: $f(x_2^+ \leq y_d^+, x_2^+ \geq 2Re_\tau - y_d^+) = 1$, $f(y_d^+ < x_2^+ < 2Re_\tau - y_d^+) = 0$. The control input can be varied by modifying Φ^+, and the damping layer thickness, y_d^+.

First, the influence of the damping layer thickness is investigated with the virtual control loop given by equation (1). To evaluate the drag reducing performance of the present control, it is compared with the virtual feedback control scheme by Iwamoto et al. (2005), which damps all turbulence fluctuations in a thin region adjacent to the wall. The latter three dimensional damping serves as a reference for the present investigation with one dimensional damping and will be referred to as 3D-damping throughout the paper.

4.2. Results

Figure 2 shows the time trace of the friction coefficient, c_f, with a damping layer thickness of $y_d^+ = 5$ and different strength factors of the damping force (given by $1/\Phi^+$). In the case of weak damping, an increase in the strength factor results in a monotonic decrease of the skin friction. For stronger forcing ($(\Phi^+)^{-1} > 2/3$), R asymptotically converges to:

$$R = 1 - (c_f/c_{f,0}) \approx 29\%. \tag{9}$$

This result shows that only damping of the spanwise velocity component in the absolute vicinity of the wall is sufficient to achieve substantial drag reduction. Even for a forcing layer thickness of $y_d^+ = 2.5$, drag reduction of almost 20% is possible. With increasing the damping layer thickness, drag reduction increases up to $y_d^+ = 30$, where relaminarization of the flow field is observed.

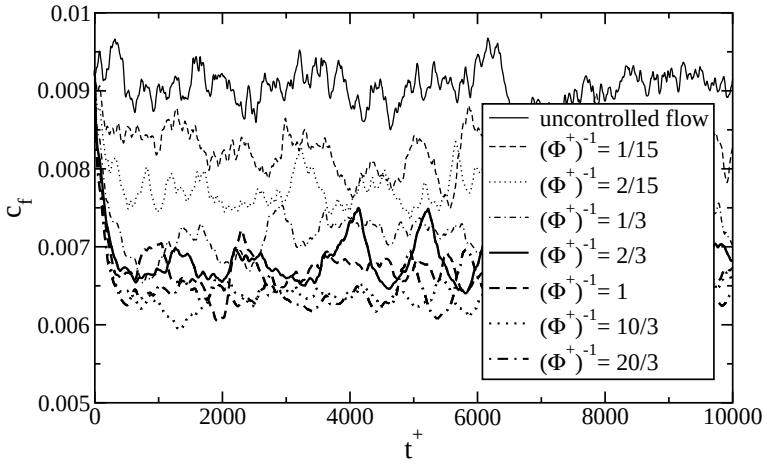

Figure 2: Time traces of the c_f-value for a channel flow with a damping layer thickness of $y_d^+ = 5$.

Based on the FIK identity (Fukagata et al., 2002), Iwamoto et al. (2005) presented a theoretical correlation between drag reduction, the Reynolds number, Re_τ, of the uncontrolled flow and the relative thickness of the damping layer, y_d/δ, in which the flow is forced to be laminarized. The above value of $R = 29\%$ coincides with this estimation of drag reduction for 3D-damping in a damping layer $y_d^+ = 5$ at $Re_\tau = 150$. The same agreement between strong damping of the spanwise velocity component and 3D-damping is found for a variety of damping layer thicknesses.

Figure 3 shows the Reynolds stresses in the controlled flows with damping force strength factors of $(\Phi^+)^{-1} = 1/15$ and $2/3$, and a damping layer thickness of $y_d^+ = 10$. They are compared with the uncontrolled channel flow and the controlled flow of the 3D-damping. In these plots, all variables are normalized by the wall shear velocity of the corresponding flow.

Throughout the paper a normalization with the inner variables of the uncontrolled flow ($u_{\tau,0}$), will be denoted with the superscript $^+$, while normalization with the inner variables of the controlled flow (u_τ) will be denoted with $'$:

$$u^+ = \frac{u}{u_{\tau,0}},\ y^+ = \frac{y u_{\tau,0}}{\nu} \text{ and } u' = \frac{u}{u_\tau},\ y' = \frac{y u_\tau}{\nu}. \tag{10}$$

The comparison of data in $^+$-normalization allows to directly compare the magnitude of different components which are all obtained for simulations

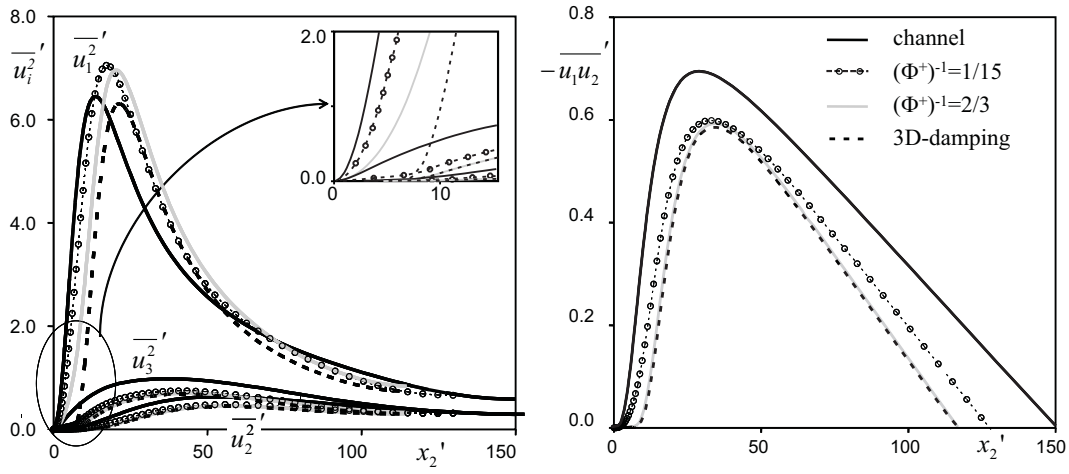

Figure 3: Reynolds stresses of controlled flows ($y_d^+ = 10$) in comparison with the Reynolds stresses of the uncontrolled channel flow and of the 3D-damping case (Iwamoto et al., 2005). The dash, $()'$, indicates that the normalization is based on the inner variables of each controlled flow.

at the same bulk Reynolds number. The $'$-normalization is more suitable when considering Reynolds number effects that occur due to a change in the friction Reynolds number, $Re_\tau = u_\tau \delta/\nu$, for the controlled flow.

From figure 3 it can be seen that the active damping of the spanwise velocity fluctuation also induces damping of the wall-normal velocity component. In the case of strong damping, the spanwise and wall-normal Reynolds stresses coincide with the 3D-damping case. The same holds for the Reynolds shear stress, $\overline{u_1 u_2}$. This fact suggests that the theoretical drag reduction predicted by Iwamoto et al. (2005) should also hold for the present control. The drag reduction predicted in their study shows that the drag reduction due to the suppression of $\overline{u_1 u_2}$ in the damping layer exhibits only weak Reynolds number dependence. We found the same behavior for $Re_\tau = 300$ and 450. Since the theoretical predictions of Iwamoto et al. (2005) show a weak Reynolds number influence up to Reynolds numbers of engineering interest, it is expected that the present control scheme will also work at higher Reynolds numbers.

A difference between the present control and 3D-damping of all three velocity components within the damping layer appears in the streamwise velocity fluctuation. For the present control a reduction of the corresponding

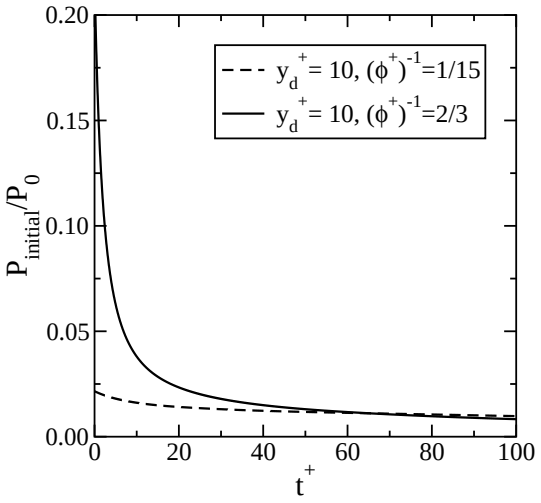

Figure 4: Time trace of the initial control power input, $P_{initial}$, normalized by the pumping power of the uncontrolled channel flow, P_0.

Reynolds stress, $\overline{u_1 u_1}'$, in the near-wall region can be observed, but it remains significantly higher than that in the 3D-damping reference case. The peak values of $\overline{u_1 u_1}'$ increase for the present control scheme indicating that the resulting flow field is different from an uncontrolled flow at the same friction Reynolds number. For a scaling based on the inner variables of the uncontrolled flow $\overline{u_1 u_1}^+$ decreases when the control is applied.

The results are in agreement with the results of SK and LK and indicate that the turbulent kinetic energy that remains in the flow field is higher in the present control than in the 3D-damping case. Since the same amount of drag reduction is achieved, high net energy saving rates are possible with w-damping. Figure 4 shows the time trace of the initial space averaged power input, $P_{initial}$, for the current idealized feedback control in relation to the pumping power for the uncontrolled flow case, P_0. It can be seen that $P_{initial}/P_0$ decays rapidly within $t^+ = 100$ from the value at $t^+ = 0$ which is 2% or 20% (depending on the strength factor of the applied forcing) to values below 1% indicating the high potential of the present control scheme for achievement of large S and G values. An equilibrium state, in which the power input does not decrease further, is reached for $t^+ > 1000$. All statistical results presented in this paper are obtained by taking statistics for $t^+ > 1000$.

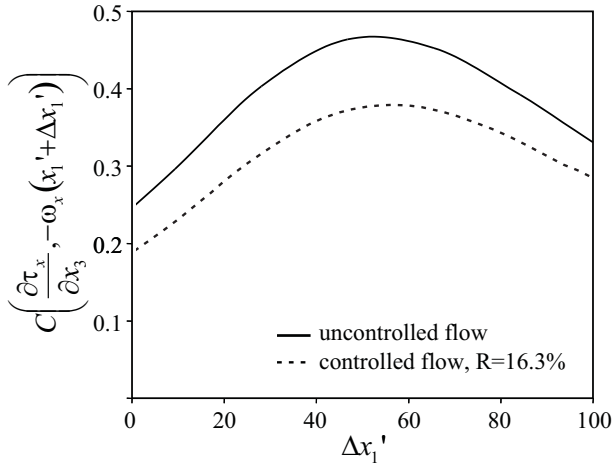

Figure 5: Spatial correlation, C, between the spanwise gradient of the streamwise wall shear stress, $\partial\tau_x/\partial x_3$, and the negative streamwise vorticity , $-\omega_x$, at different downstream locations for an uncontrolled channel flow and a controlled flow according to equation (11). The normalization is based on the inner variables of each flow.

5. Closed Loop Control Based on the Streamwise Wall Shear Stress

In the idealized feedback loop, instantaneous velocity information and local introduction of a body force at every location in the damping layer are required. Since this assumption is unrealistic, it is desirable to develop a control algorithm with a finite number of arrayed sensors and actuators placed on the channel walls.

The instantaneous spanwise wall shear stress, τ_z, is well known to be useful for state estimation of wall turbulence and LK demonstrated that it is also an appropriate sensor control input for w-damping with continuous sensing and actuation. However, it is difficult to measure τ_z in practice because of the diminishing scales of turbulence toward the wall (Suzuki and Kasagi, 1992). Therefore, we focus on the streamwise wall shear stress, τ_x, which can reliably be measured on a channel wall, as sensing quantity.

The instantaneous streamwise wall shear stress is strongly influenced by the presence of near-wall streaks. From the regeneration cycle of near-wall turbulence (Hamilton et al., 1995), it is known that near-wall streaks are not simply caused by the streamwise vortices, but in turn the breakdown of streaks will lead to regeneration of the streamwise vortices. Underneath a streamwise vortex significantly large spanwise velocity fluctuations are in-

duced. Therefore, the knowledge of the location and swirl direction of a streamwise vortex would enable the required damping of the spanwise velocity fluctuation.

Typical near-wall streaks are characterized by a spanwise gradient of the streamwise wall shear stress, τ_x, due to the fact that low and high speed streaks mostly occur in pairs. Therefore, we investigate the streamwise two-point correlation between $\partial\tau_x/\partial x_3$ and the streamwise vorticity, ω_x, at $x_2^+ = 15$. The correlation is plotted as the solid line in figure 5. It can clearly be seen that the strongest correlation of almost 0.5 is located about 50 viscous length units downstream of the sensing location. The correlation might be influenced by the structural asymmetry of low and high speed streaks, the statistical nature of these structures or streak meandering. The streamwise distance for the maximum correlation is in agreement with the results of Endo et al. (2002), who employed conditional averaging to investigate the spatial relation between streamwise vortices and meandering near-wall streaks. In the following it will be used for the formulation of an active control loop where sensors are placed upstream of the actuator.

Figure 6 shows the conditionally averaged flow field for $\partial\tau_x/\partial x_3 > 1.5(\partial\tau_x/\partial x_3)_{rms}$ at $\Delta x_1^+ = 50$ downstream of the sensing location. A streamwise vortex with clockwise rotation is located at this position. The analysis of different downstream locations in the conditionally averaged flow field reveals that a streamwise vortex which is tilted away from the wall exists downstream of the sensing location.

Based on the obtained results we propose an actuator input that depends on the upstream spanwise gradient of the streamwise wall shear stress, $\partial\tau_x/\partial x_3$. In general, body forces can be introduced through Lorentz forces in electrically conducting fluids or through plasma actuators in air. These forces will decay from a maximum value at the wall. In order to mimic such a body force distribution, bf_3 is assumed to decay linearly from a finite value at the wall (determined by $(\Phi^+)^{-1}$) to zero at the edge of the forcing layer ($x_2^+ = y_d^+$). In the present investigation the forcing layer thickness is fixed to $y_d^+ = 10$. The resulting body force thus reads:

$$bf_3^+(x_1^+, x_2^+, x_3^+) = \frac{f(x_2^+)}{\Phi^+}(y_d^+ - x_2^+) \cdot \frac{\partial\tau_x^+}{\partial x_3^+}(x_1^+ - \Delta x_1^+, x_3^+). \qquad (11)$$

The dotted line in figure 5 shows the correlation between $\partial\tau_x/\partial x_3$ and the streamwise vorticity at $x_2^+ = 15$ for the controlled flow according to equation

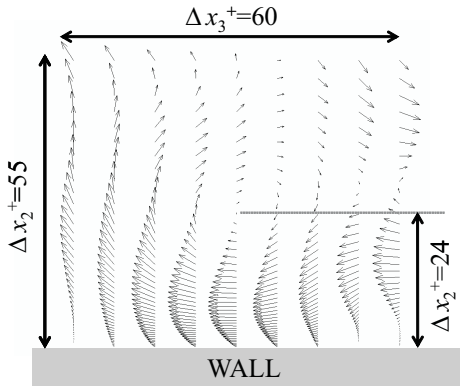

Figure 6: Conditionally sampled flow field at $\Delta x_1^+ = 50$ behind the measuring location.

(11) when $R = 16.3\%$. While the value of the correlation is slightly reduced, the position of the strongest correlation remains at the same streamwise distance as in the uncontrolled flow. This result suggests that the upstream sensing of $\partial\tau_u/\partial x_3$ can also be applied in controlled flows to identify the existence and rotational direction of streamwise vortices. Therefore, we set the streamwise distance between sensors and actuators to be $\Delta x_1^+ = 50$ hereafter, unless otherwise stated. The effects of Δx_1^+ on the control performance will be discussed in Sec. 6.

The effect of varying forcing strength, $(\Phi^+)^{-1}$, on the net energy saving rate, S, and energy gain, G, is shown in figure 7 for different Reynolds numbers. Due to the high gain in the present control, R and S are almost identical. Up to $(\Phi^+)^{-1} \approx 0.6$, the net energy saving rate and energy gain increase with increasing forcing strength. For $Re_\tau = 300$ and 450 higher forcing strength is required to reach a certain net energy saving rate. Therefore, the corresponding energy gain is lower. While the Reynolds number effect is pronounced when comparing results at $Re_\tau = 150$ and 300, it is much weaker for a further increase of the Reynolds number to $Re_\tau = 450$. We may thus expect that high values of R and S are kept even at higher Reynolds numbers.

A further increase of the forcing strength for $Re_\tau = 150$ reveals that G decreases rapidly while S varies only slightly. This effect can be explained by investigating the details of the power input and the flow field for controlled cases with high forcing strength.

The power input, as defined by equation (4), is given by the product of

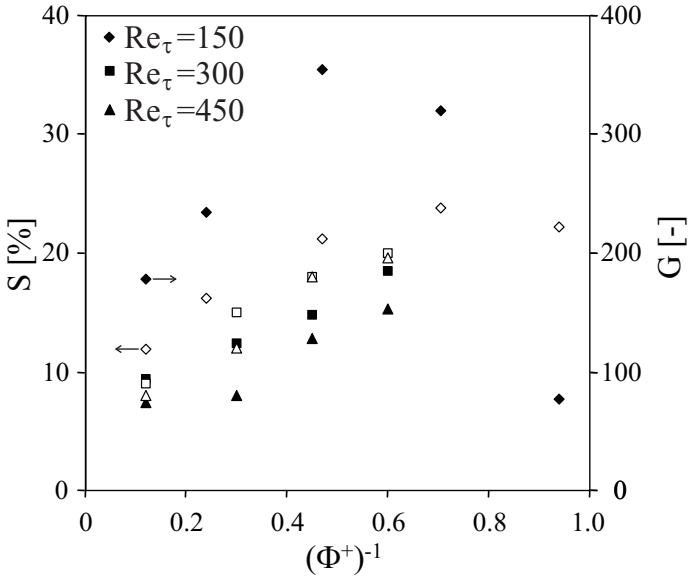

Figure 7: Effect of the forcing strength $(\Phi^+)^{-1}$ on S (open symbols) and G (solid symbols) for the flow control loop given by equation (11) with $\Delta x_1^+ = 50$ at different Reynolds numbers.

the body force, bf_3, and the spanwise velocity fluctuation, $u_3 = w$. Therefore, the local power input, P_3, is negative if the body force acts as a damping force and positive if it acts as a w-enhancing force. Note that P_{in} as given in equation (4) is based on the absolute value of P_3 in order to obtain a conservative estimate of the control power input.

Figure 8 depicts the local power input, P_3, due to the applied body force as a function of wall distance for the same control settings as discussed in figure 6. For small forcing strengths P_3 assumes negative values only, indicating that the body force (in spatial average, see equation (4)) acts as a damping force throughout the entire forcing layer. For stronger forcing, positive values of P_3 can be found in the vicinity of the wall while P_3 remains negative in the outer region of the forcing layer. Since the applied body force does not change its sign within the forcing layer, the change of sign for P_3 can only be attributed to a directional change of the spanwise velocity fluctuations within the forcing layer. In this "reversed region" fluctuations are now not damped but enhanced by the applied body force.

Figure 9 shows the corresponding Reynolds stresses (close loop control

with strong forcing of $(\Phi)^{-1} = 0.94$) in comparison to those in the uncontrolled channel flow. It reveals that the spanwise velocity fluctuations are decreased at the outer edge of the forcing layer but, in contrast to the intention of the applied control, the spanwise velocity fluctuations are increased in the absolute vicinity of the wall. This behavior is in agreement with the above discussion of the local power input.

The visualization of a typical streamwise vortex in the corresponding flow field, as shown in the bottom right corner of figure 9, provides an insight to what is happening in the wall vicinity due to the applied strong forcing. It can be seen that the spanwise flow at the lower side of the streamwise vortex has not only been damped as intended by the applied control but the flow direction has been reversed. This flow reversal in the wall vicinity seems to occur whenever the body force, bf_3, which has its maximum value at the wall, exceeds a certain limit.

Since only damping of the spanwise velocity fluctuation is required for the flow control to be successful, it can be stated that for strong forcing the body force is unnecessarily strong in the near wall region such that the local power input cannot be used optimally. As a result the gain decreases and thus there exists an optimal strength, $(\Phi^+)^{-1}$, of the body force with respect to energy gain. It is noted that with further increase of the forcing strength, the simulation could not be continued due to numerical instability.

As observed in the ideal w-damping control, the wall-normal velocity component in figure 9 behaves similarly to the spanwise one and also increases in the very near-wall region. Despite this increase, $\overline{u_1 u_2}$, which determines R (Fukagata et al. 2002), is reduced within the entire forcing layer and has the same distribution as in the ideal w-damping case for the same drag reduction (not shown here). This behavior can be attributed to reduction of $\overline{u_1 u_1}$ and decrease of the correlation between the u_1 and u_2 fluctuations within y_d^+.

Figure 10 shows a comparison between instantaneous flow fields under the uncontrolled and controlled conditions. The grey shading indicates the magnitude of the streamwise velocity at $x_2^+ = 5$, while the core of a streamwise vortex is identified with a threshold in the second invariant of the deformation tensor. For the controlled flow, the normalization is made by the inner variables of the uncontrolled and also the controlled flow.

The uncontrolled and controlled flows visualized with the same threshold of uncontrolled flow variables clearly show that the turbulence activity is actually much reduced by the control under the same flow rate condition. We can see the drastically decreased number of vortical structures, which is

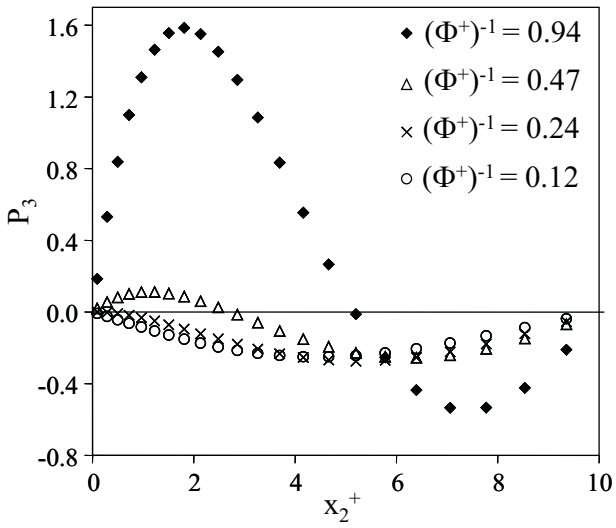

Figure 8: Local power input, P_3, as a function of wall distance for different forcing strengths.

associated with the observed drag reduction.

If the visualization is based on normalization with the inner variables of the controlled flow, the size of the vortex core regions appears larger. Furthermore, additional smaller streamwise vortices become visible. In comparison to the uncontrolled flow, the number of streamwise vortices visualized by II' is not clearly reduced. However, it can still be observed that the typical streamwise vortices are slightly elongated and spaced apart wider, indicating that the controlled flow shows a slight structural difference from an uncontrolled flow at lower Reynolds number.

6. Effect of Finite Actuator Size

In order to further develop the control scheme towards a realistic system, the effect of finite actuator size needs to be taken into account. Up to now the actuation was assumed to be continuous on top and bottom wall with sensor information available at every grid point and for every time step. Hence, in this ideal simulation, the spatial and temporal resolutions are fine enough to capture all essential scales of turbulence. A practical flow control scheme will require sensors and actuators with certain physical dimensions, spacing and

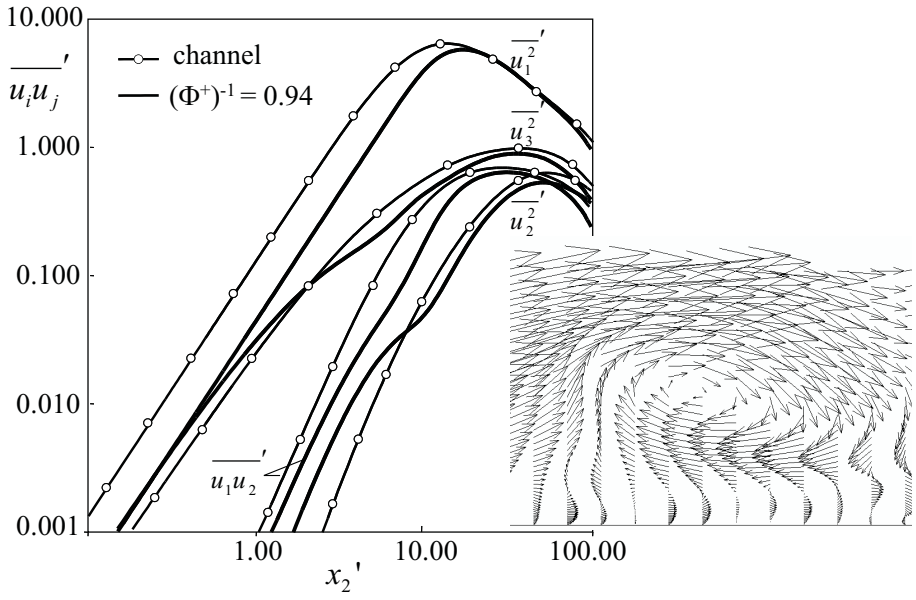

Figure 9: Reynolds stresses for a controlled flow according to equation (11) in comparison to an uncontrolled channel flow and a typical streamwise vortex of the controlled flow field. The normalization is based on the respective inner variables.

bandwidth. The investigations and results discussed in the following present a first step in this direction.

The correlation displayed in figure 5 suggests that drag reduction can be obtained for a range of distances between sensor and actuator, Δx_1^+. Therefore, a parametric study is performed and the influence of Δx_1^+ on the drag reduction performance is investigated. Simulations are repeated for four different forcing strengths.

For the two stronger forcing cases, which are characterized by positive values of P_3 in the near wall region, drag reduction can only be achieved for limited values of Δx_1^+. Note that Δx_1^+ is normalized by the inner variables of the uncontrolled flow. For $(\Phi^+)^{-1} = 0.24$ and 0.12 all simulations up to a spacing of $\Delta x_1^+ \approx 200$ result in drag reduction. In these simulations the local energy input, P_3, shows negative values throughout the entire forcing layer.

Figure 11 shows the dependence of S on Δx_1^+ for all four forcing strengths. Only the cases for which drag reduction was obtained are included. While there is no clear tendency for the weakest forcing strength, the other three

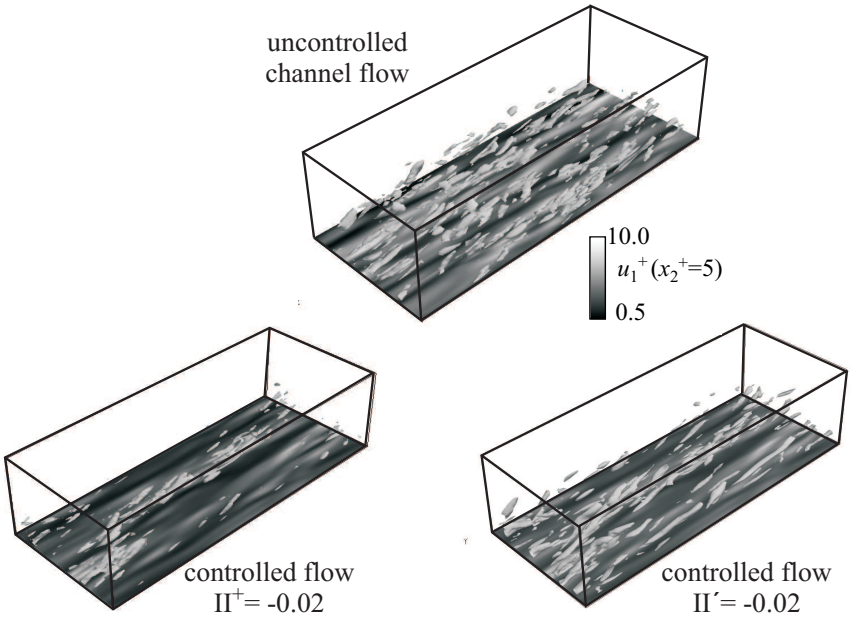

Figure 10: Flow visualization of the uncontrolled channel flow at $Re_\tau = 150$ (top) and the controlled case ($S = 17.6\%$) according to equation (11) (bottom). The visualization of the streamwise vortices is based on isosurfaces of the second invariant of the deformation tensor, where the normalization is based on the inner variables of the uncontrolled flow, $II^+ = -0.02$, and the inner variables of the controlled flow, $II' = -0.02$, respectively.

cases show a maximum drag reduction at a certain streamwise distance, $(\Delta x_1^+)_{max}$. $(\Delta x_1^+)_{max}$ decreases with increasing forcing strength. For $(\Phi^+)^{-1} = 0.24$ it can be seen that an almost constant value of $S \approx 17\%$ is obtained over a wide range. The maximum value of $S = 17.6\%$ is located at $\Delta x_1^+ = 84$, which corresponds to $\Delta x_1' = 76$ if normalized with the inner variables of the controlled flow.

The results for $Re_\tau = 450$ with $(\Phi^+)^{-1} = 0.60$ are also included in Fig. 11. As discussed in respect to Fig. 7, higher forcing strength is required to achieve the same R or S at higher Reynolds number. With increasing Δx_1^+ from 30 to 70, S is gradually increased up to $S \sim 20\%$, then suddenly falls down to $S \sim 10\%$ at $\Delta x_1^+ = 100$. The Reynolds number dependence of the optimal streamwise distance between sensors and actuators will be investigated further in future work.

The present results suggests that the streamwise distance between sen-

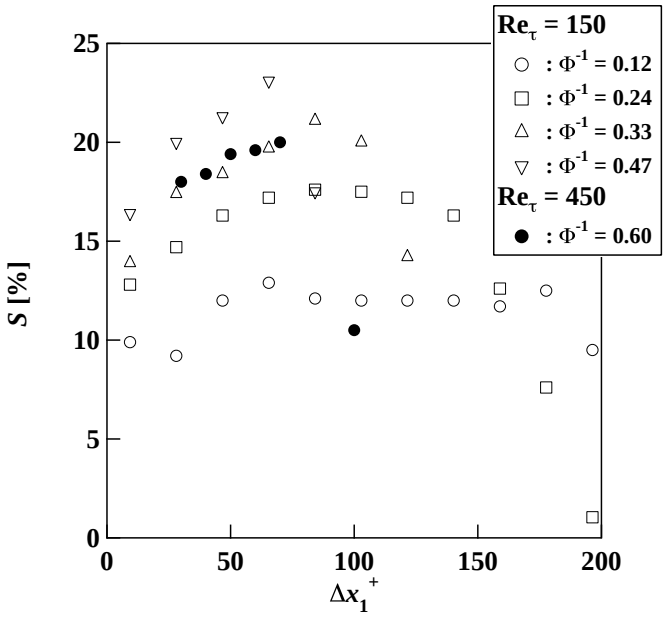

Figure 11: Influence of the streamwise distance, Δx_1^+, between sensor and actuator on the net energy saving rate, S, for different forcing strength, $(\Phi^+)^{-1}$.

sors and actuators should be in the order of 100 in the wall units of the uncontrolled flow. Therefore, it is reasonable to chose the length of a finite size actuator in this order.

Since the maximum net energy saving rate for $Re_\tau = 150$ is obtained for $\Delta x_1^+ = 84$, the center of actuators with finite size length is placed at this location. Actuator lengths of $\Delta x^+ = 37$, 75 and 150 viscous units are tested. In these simulations the actuation is still continuous on both channel walls but the number of sensors is reduced such that spanwise rows of sensors are placed at streamwise distances that correspond to the actuator length.

These simulations result in $S = 18.5\%$, 18.5% and 18.2%, respectively, suggesting that the streamwise extension of the actuator up to the given dimensions has no significant effect on the obtained net energy saving rate while the energy saving due to the applied control is at least two orders of magnitude larger than the energy input, i.e. $G > 100$.

The limitations for a spanwise extension of the actuator are much stricter. If a finite spanwise extend of $\Delta z^+ = 22$ and $\Delta z^+ = 37$ viscous units is applied to the actuators with $\Delta x^+ = 75$, the energy saving rate is reduced

to $S = 13.4\%$ and $S = 9.0\%$, respectively. For actuators with $\Delta x^+ = 150$ the corresponding values are $S = 12.2\%$ for $\Delta z^+ = 22$ and $S = 8.4\%$ for $\Delta z^+ = 37$.

In the latter case top and bottom wall of the channel are covered with 96 actuators and twice the number of streamwise wall shear stress sensors. These sensors are placed in front of the actuator in pairs for which the spanwise separation is given by 15 viscous units of the uncontrolled flow.

The influence of actuator spacing and bandwidth has not yet been considered and will be investigated in future work.

7. Conclusion

The present investigation demonstrates that the suppression of the spanwise velocity component in the near-wall region results in essentially the same control effect as that obtained by 3D-damping. Since the Reynolds number effect on drag reduction achieved by 3D-damping was found to be weak (Iwamoto et al., 2005), we may expect that control schemes based on w-damping will also work at high Reynolds numbers. However, since larger forcing strength is required to attain the same drag reduction at higher Reynolds number, the gain tends to decrease with increasing the Reynolds number.

A novel control loop which is designed to damp the spanwise velocity fluctuations in the downstream near-wall region is proposed. The sensor input is given by the spanwise gradient of the streamwise wall shear stress, $\partial\tau_x/\partial x_3$, up to $\Delta x_1^+ = 200$ viscous units upstream of the actuator. At low forcing strength, the effect of Δx_1^+ on R and S is minor. With increasing the forcing strength, however, the optimal Δx^+ gradually decreases and the control performance rapidly deteriorates beyond the optimal Δx_1^+.

The present control loop is considered to be of practical importance, because the streamwise wall shear stress is easier to measure than the spanwise one (Suzuki and Kasagi, 1992) and also the sensor placement in a range of upstream locations is possible. As for the former, the drag reduction achieved in the present control algorithm is up to 20%, which is the highest value obtained by the existing control algorithms based on the streamwise-wall shear stress only. The latter enables the use of actuators with large streamwise extension. While the streamwise extension of the actuators is found to have a weak influence on drag reduction and net energy saving rate, the spanwise extension seems to have stronger limitations. An important feature of the

proposed control loop is the high energy gain which can be optimized based on the control strength.

References

[1] Choi, H., Moin, P., Kim, J., 1994. Active turbulence control for drag reduction in wall bounded flows. J. Fluid Mech., 262, 75-110.

[2] Endo, T., Kasagi, N., Suzuki, Y., 2000. Feedback control of wall turbulence with wall deformation. Int. J. Heat and Fluid Flow, 21, 568-575.

[3] Fukagata, K., Iwamoto, K., Kasagi, N., 2002. Contribution of Reynolds stress distribution to the skin friction in wall-bounded flows. Phys. Fluids, 14, L73-L76.

[4] Fukagata, K., Kasagi, N., 2004. Suboptimal control for drag reduction via suppression of near-wall Reynolds shear stress. Int. J. Heat and Fluids Flow, 25, 341-350.

[5] Hamilton, J.M., Kim, J., Waleffe, F., 1995. Regeneration mechanism of near-wall turbulence structures. J. Fluid Mech., 287, 317-348.

[6] Iwamoto, K., Fukagata, K., Kasagi, N., Suzuki, Y., 2005. Friction drag reduction achievable by near-wall turbulence manipulation at high Reynolds number. Phys. Fluids, 17, 011702.

[7] Iwamoto, K., Suzuki, Y. and Kasagi, N., 2002. Reynolds number effects on wall turbulence: Toward effective feedback control, Int. J. Heat Fluid Flow 23, 678-689.

[8] Kasagi, N., Suzuki, Y., and Fukagata, K., 2009. Microelectromechanical Systems-Based Feedback Control of Turbulence for Skin Friction Reduction. Annu. Rev. Fluid Mech., 41, 231-251.

[9] Kim, J., Moin, P. and Moser, R. D., 1987. Turbulence statistics in fully developed channel flow at low Reynolds number, J. Fluid Mech. 177, 133-166.

[10] Koumoutsakos, P., 1999. Vorticity flux control for a turbulent channel flow. Phys. Fluids, 11, 248-250.

[11] Morimoto, K., Iwamoto, K., Suzuki, Y., Kasagi, N., 2002. Genetic algorithm-based optimization of feedback control scheme for wall turbulence. Proc. 3rd Symp. Smart Control of Turbulence, Tokyo, 107-113.

[12] Moser, R. D., Kim, J., Mansour, N. N., 1999. Direct numerical simulation of turbulent channel flow up to $Re_\tau = 590$. Phys. Fluids 11, 943-945.

[13] Lee, C., Kim, J., Babcock, D., Goodman, R., 1997. Application of neural networks to turbulence control for drag reduction. Phys. Fluids, 9, 1740-1747.

[14] Lee, C., Kim, J., Choi, H., 1998. Suboptimal control of turbulent channel flow for drag reduction. J. Fluid Mech., 358, 245-258.

[15] Lee, C., Kim, J., 2002. Control of the viscous sublayer for drag reduction. Phys. Fluids, 14, 2523-2529.

[16] Satake, S., Kasagi, N., 1996. Turbulence control with wall-adjacent thin layer damping spanwise velocity fluctuations. Int. J. Heat Fluid Flow, 17, 343-352.

[17] Suzuki, Y., Kasagi, N., 1992. Evaluation of hot-wire measurement in wall shear turbulence using a direct numerical simulation database. Experimental Thermal and Fluid Science, 5, 69-77.